ADVANCED MATERIALS
www.advmat.de

A Print-and-Fuse Strategy for Sacrificial Filaments Enables Biomimetically Structured Perfusable Microvascular Networks with Functional Endothelium Inside 3D Hydrogels

Matthias Ryma, Hatice Genç, Ali Nadernezhad, Ilona Paulus, Dominik Schneidereit, Oliver Friedrich, Kristina Andelovic, Stefan Lyer, Christoph Alexiou, Iwona Cicha, and Jürgen Groll**

A facile and flexible approach for the integration of biomimetically branched microvasculature within bulk hydrogels is presented. For this, sacrificial scaffolds of thermoresponsive poly(2-cyclopropyl-2-oxazoline) (P*cyclo*PrOx) are created using melt electrowriting (MEW) in an optimized and predictable way and subsequently placed into a customized bioreactor system, which is then filled with a hydrogel precursor solution. The aqueous environment above the lower critical solution temperature (LCST) of P*cyclo*PrOx at 25 °C swells the polymer without dissolving it, resulting in fusion of filaments that are deposited onto each other (print-and-fuse approach). Accordingly, an adequate printing pathway design results in generating physiological-like branchings and channel volumes that approximate Murray's law in the geometrical ratio between parent and daughter vessels. After gel formation, a temperature decrease below the LCST produces interconnected microchannels with distinct inlet and outlet regions. Initial placement of the sacrificial scaffolds in the bioreactors in a pre-defined manner directly yields perfusable structures via leakage-free fluid connections in a reproducible one-step procedure. Using this approach, rapid formation of a tight and biologically functional endothelial layer, as assessed not only through fluorescent dye diffusion, but also by tumor necrosis factor alpha (TNF-α) stimulation, is obtained within three days.

1. Introduction

The growing awareness of the limitations of conventional 2D cell culture techniques gave rise to an expanding interest in 3D tissue models, which enable obtaining more accurate results, particularly in biology, medicine and pharmacy. This relies primarily on creating a more realistic cell environment since cell–cell and cell–matrix interactions in 3D models are more comparable to the in vivo conditions.[1,2] Additionally, these artificial 3D tissues may potentially be used as tissue replacement for regenerative medicine.[3]

There is a critical challenge in creating artificial 3D tissue models larger than 0.6–1 mm, depending on the matrix and cell density. According to the in vitro measurements in 3D spheroids reported by Grimes et al.[4], the upper limit of the oxygen diffusion distance of 232 ± 22 µm was observed experimentally. In larger tissue models, the supply of oxygen and nutrients cannot be ensured by osmosis, leading to a necrotic core generation.[5] In vivo, the vascular system guarantees the nutrient supply through a complex network of large arteries branching into smaller vessels and capillaries.[6] To overcome this size limitation in artificial tissues or cell-based organoids exceeding a certain thickness, it is necessary to generate microchannel networks to keep cells alive by supplying oxygen and nutrients. The microchannel networks must be perfused

M. Ryma, A. Nadernezhad, I. Paulus, J. Groll
Chair for Functional Materials for Medicine and Dentistry at the Institute for Functional Materials and Biofabrication (IFB) and Bavarian Polymer Institute (BPI)
University of Würzburg
Pleicherwall 2, 97070 Würzburg, Germany
E-mail: juergen.groll@fmz.uni-wuerzburg.de

The ORCID identification number(s) for the author(s) of this article can be found under https://doi.org/10.1002/adma.202200653.

DOI: 10.1002/adma.202200653

H. Genç, S. Lyer, C. Alexiou, I. Cicha
Section of Experimental Oncology and Nanomedicine (SEON)
Else Kröner-Fresenius-Stiftung-endowed Professorship for Nanomedicine
ENT Department
Universitätsklinikum Erlangen
Friedrich-Alexander-Universität Erlangen-Nürnberg
Glueckstr. 10a, 91054 Erlangen, Germany
E-mail: iwona.cicha@uk-erlangen.de

D. Schneidereit, O. Friedrich
Institute of Medical Biotechnology
Friedrich-Alexander-Universität Erlangen-Nürnberg
Ulrich-Schalk-Str. 3, 91056 Erlangen, Germany

K. Andelovic
(Chair of) Experimental Biomedicine II
University Hospital Würzburg
Josef-Schneider-Straße 2, 97080 Würzburg, Germany

with media through a perfusion pump or other flow-inducing systems to ensure oxygen and nutrient supply, as well as metabolic waste removal.

The state-of-the-art technologies for the generation and utilization of reproducible microchannels are based on "organ-on-a-chip" (OoC) systems, which allow the emulation of physiological reactions of organ-like systems via connection to microfluidic systems.[7] Although OoC systems provide channel structures, they are only a part of an artificial molded container to which cells are attached. Furthermore, cell populations such as endothelial cells are divided by permeable membranes from other cell populations, which may inhibit both the mechanical stimuli and the direct interactions between different cell types. While the OoC system proved to be a valuable research tool in studying cellular metabolism and drug screening, their inherent limitation in mimicking the 3D cellular microenvironment has impacted their potential for creating large 3D tissues.

An artificial 3D matrix should mimic the complex cellular interactions and facilitate cell attachment, survival, and proliferation in a 3D environment. Hydrogels are of particular interest in this context since they can provide a permeable microenvironment, which can be further physically and chemically tuned based on particular needs. Despite the aqueous nature of hydrogel matrices, limitations based on diffusion distance demand the adaptation of microvascular systems into such 3D microenvironments.

During the past decade, advances in manufacturing technologies enabled the creation of complex 3D microvascular systems, and in particular, approaches based on additive manufacturing (AM) gained much attention in recent years. Among different AM technologies, 3D bioprinting allowed the generation of in situ microchannels within 3D-hydrogel constructs containing cells. In this way, the microchannels can either be created by introducing empty spaces during printing or by deposition of sacrificial inks, which can be removed afterward. Among other methods, techniques including extrusion-based printing,[8] in-gel printing,[9] and stereolithography[10] were reported. However, these methods were mainly limited by the low resolution, the need to adapt hydrogel properties to the process criteria, and the shear-related cell viability issues.[11] In particular, the direct ink writing of templating fugitive inks extensively explored by the group of J. Lewis aimed to expand the scopes of printability and functionality of sacrificial templating by taking advantage of relatively easy-to-handle thermoresponsive sacrificial inks based on pluronics and gelatin.[12,13] This approach has further evolved to the direct sacrificial writing into functional tissues (SWIFT) by creating a sacrificial template within organ-specific and high-density cellular aggregates.[14]

Alternatively, methods based on templating microchannels have been developed, using sacrificial structures separately 3D-printed and subsequently embedded in hydrogel matrices. The rationale behind this new trend was mainly addressing the size, and more importantly, spatial limitations of the direct writing approach. The initial reports on this technique were based on embedding 3D-printed carbohydrate-based microfibers within the bulk hydrogel matrices.[15,16] Although this approach could potentially improve the resolution and freedom of the design in creating microchannels, two main challenges still needed to be addressed. The sacrificial structures based on carbohydrates readily dissolve in an aqueous environment, making the embedment of sacrificial scaffolds impossible in almost any hydrogel matrix without loss of their geometrical features. Post-processing methods such as coating with polymers, hydrogels, or other materials are often required to increase the timeframe of gelation, increasing the difficulty with the increasing complexity of the scaffold.[17,18] Furthermore, the high hygroscopicity of carbohydrate sugars limit scaffolds' storability in standard room conditions.

More importantly, while the majority of the studies focused on developing case-specific methods of creating microchannels, none thus far tried to propose efficient methodologies for integrating the microchannels into perfusion systems. Most of the reported efforts were focused on the post-fabrication creation of in- and outlet regions by manual insertion of microneedles. Considering the small dimensions of the formed channels, especially in microvascular systems, the precision of embedment of the sacrificial scaffolds and establishing a closed perfusion loop is of tremendous importance. In this way, two main aspects in producing a functional microvascular model could be identified, which include: a) methodologies for fabrication of microchannels; and b) their further integration into a perfusion system to enable the biological functionality of the created microvasculature.

By considering these two aspects, this study addresses the challenges in fabricating perfusable and functional microvascular structures by developing a novel approach based on embedding thermoresponsive sacrificial scaffolds made from poly(2-cyclopropyl-2-oxazoline) (P*cyclo*PrOx) integrated within a custom-designed, adaptable bioreactor. The sacrificial P*cyclo*PrOx structures with dimensions in the microvasculature range were produced by melt electrowriting (MEW).[19] The precise positioning and fixation of the sacrificial scaffolds at the inlet and outlet of a newly developed bioreactor enabled blockage-free casting of the hydrogel matrix within the perfusion chamber, ensuring that the channels remain perfusable. P*cyclo*PrOx scaffolds with lower critical solution temperature (LCST) of 25 °C were removed simply by a short incubation below the room temperature, providing enough time for gelation of the hydrogel matrix through a fully biocompatible process. Compared with state of the art in literature such as SWIFT approach, the methodology presented here addresses the limitations in realizing low-dimension microchannels with significant flexibility in design, and a generalized solution to integrate the microchannels within the perfusion systems. The proposed methodology resulted in the one-step fabrication of microchannels fully integrated within the bioreactor, ready for subsequent endothelialization and functional assessments. We demonstrated that a functional endothelial monolayer can be created inside these channels within 72 h using a static seeding set-up followed by fluid perfusion. The advantages of this system, including adaptable channel diameters and designs, good storability at room conditions, facile removal of sacrificial structures and rapid endothelialization, could make this system an important milestone in developing vascularized tissue constructs.

2. Results

2.1. Melt Electrowriting of Sacrificial P*cyclo*PrOx Scaffolds and Their Behavior in Hydrogels

Prior to the MEW, the synthesized P*cyclo*PrOx was thoroughly characterized to confirm the desired chemistry and physical properties (Figures S1–S7, Table S1, Supporting Information). A significant advantage of the MEW is the tunability of the process, by which one can produce fiber diameters ranging over several orders of magnitudes.[20–22] We showed this capacity of MEW by following a Response Surface Methodology (RSM) design of experiments (DoE) to produce scaffolds with predictable fiber diameters. By choosing a convenient jet-forming range of the simple-to-adjust parameters, namely the applied pressure (P), the applied voltage (V) and the tip-to-collector distance (H), it was possible to construct an optimized model to predict fiber diameter (D) (Equation (1)).

$$D^{-0.39} = 0.400708 - 0.177373P - 0.004729V - 0.081932H - 0.018362PV + 0.022047PH + 0.016363VH + 0.040540P^2 \quad (1)$$

The fitted model's sanity check and the response surfaces generated for different binary combinations of process parameters are shown in **Figure 1**A–D. As expected from the literature, while the change in H imposes almost no significant change in fiber diameter, increasing P results in a significant increase in fiber diameter. In contrast, increasing V at constant P and H results in faster mass transfer, hence decreased fiber diameter. Experimental validation of the model showed that the predicted fiber diameters were within the 95% prediction interval. The details of the regression analysis and the validation results are provided in the Supporting Information. Within the range of process parameters used to build this statistical model, it was possible to fabricate bifurcated structures with average fiber diameters between 87 to 275 µm. However, it should be noted that the chosen range of process parameters was one of the possible combinations leading to the formation of the jet. Depending on the design requirements, a different range of parameters could be explored, leading to larger or smaller fiber diameters. Nevertheless, the application of RSM proved to be an efficient way to optimize and predict the diameter of P*cyclo*PrOx sacrificial scaffolds.

A simple G-code for the fabrication of sacrificial scaffolds was adapted. The details of the method for the generation of the G-code are provided in Figure S8, Supporting Information. The implemented G-code for fiber deposition was designed to resemble natural bifurcating structures (Figure 1E). In order to produce multiple bifurcation steps, the level of complexity could be further increased by a few adjustments in the G-code (Figure 1E). However, increasing the complexity also increases the susceptibility for inaccuracies, as shown in Figure 1E-iii.

In the dry state, the printed constructs retain their shape exactly as printed, and filaments deposited on top of each other remain separate filaments. However, upon hydration of melt electrowritten P*cyclo*PrOx scaffolds in an aqueous environment above the LCST, for example, by embedment in hydrogel precursors, spontaneous fusion and merging of neighboring filaments occurs (Figure 1F). The progressive softening and swelling of the fibers results in volumetric expansion, leading to the spontaneous fusion and formation of a single "parent channel" from two (or more) adjacent filaments. This process produces smooth surfaces by merging of insoluble P*cyclo*PrOx filaments inside the hydrogel matrix so that small gaps between adjacent filaments are filled by swelling P*cyclo*PrOx, unless the distance between neighboring filaments is too large. As stated above, the probability for this increases with the higher complexity of the structures (see for example Figure 1H-ix). The balance between the surface energy and viscosity of the P*cyclo*PrOx during the crosslinking of hydrogel matrix aids the formation of natural branching structures. Formation of such natural bifurcations was observed in different embedding hydrogel matrices, including gelatin-methacrylol (GelMA), agarose, alginate, and gelatin crosslinked with transglutaminase (not shown).

Reducing the temperature below 25 °C resulted in swelling and dissolution of P*cyclo*PrOx fibers. Free swelling of P*cyclo*PrOx (i.e., open inlet and outlet regions within the bulk hydrogel) resulted in rapid removal of the sacrificial scaffold without the aid of any external perfusion (Figure 1H-i–iii and Videos S1–S3, Supporting Information).

The water-induced plasticity of microfibers below the glass transition, simultaneously controlled by the increasing elasticity of the surrounding hydrogel matrix, thus resulted in the formation of bifurcated lumens, which were in good agreement with the extents of Murray's law (Figure 1G). The diameter ratio between parent and daughter microchannels created by removal of fused filaments was between the expansion ratios of 1.0 and 1.5, as defined by the ratio between the sum of the squares of the diameter of daughter microchannels and the square of the diameter of the parent microchannel (Equation (2)). This equation is derived as a measure of volume conservation during flow by considering the ratio between the area of cross-sections of the parent and daughter segments of a given channel by assuming circular lumens.

$$A_{\text{ratio}} = \frac{D_1^2 + D_2^2}{D_P^2} \quad (2)$$

The expansion ratio is a geometrical index and can be described as "a measure for the expansion in cross-section area available to flow along the microvessel from parent to daughter branches." This index is especially useful in analytical and computational solutions of the flow in microvasculatures and was preferred over a simple linear measure, as the latter does not necessarily reflect the geometrical correlations governing the branching and may not truly represent area and volume in any given segment of the microchannels with consideration of volume preservation. It must be noted that the expansion ratio as defined by Equation (2) does not, in any form, describe the swelling of P*cyclo*PrOx fibers after placement in aqueous media, but only refers to the channels that are generated in the hydrogel after dissolution of the sacrificial template. Accordingly, the values of diameters in Equation (2) refer to the diameter of microchannels, not the microfibers. This is also reflected by the color-coding in Figure 1G, which shows that the correlation between the channel diameters created by the print-and-fuse method is not dependent on the as-printed fiber diameters.

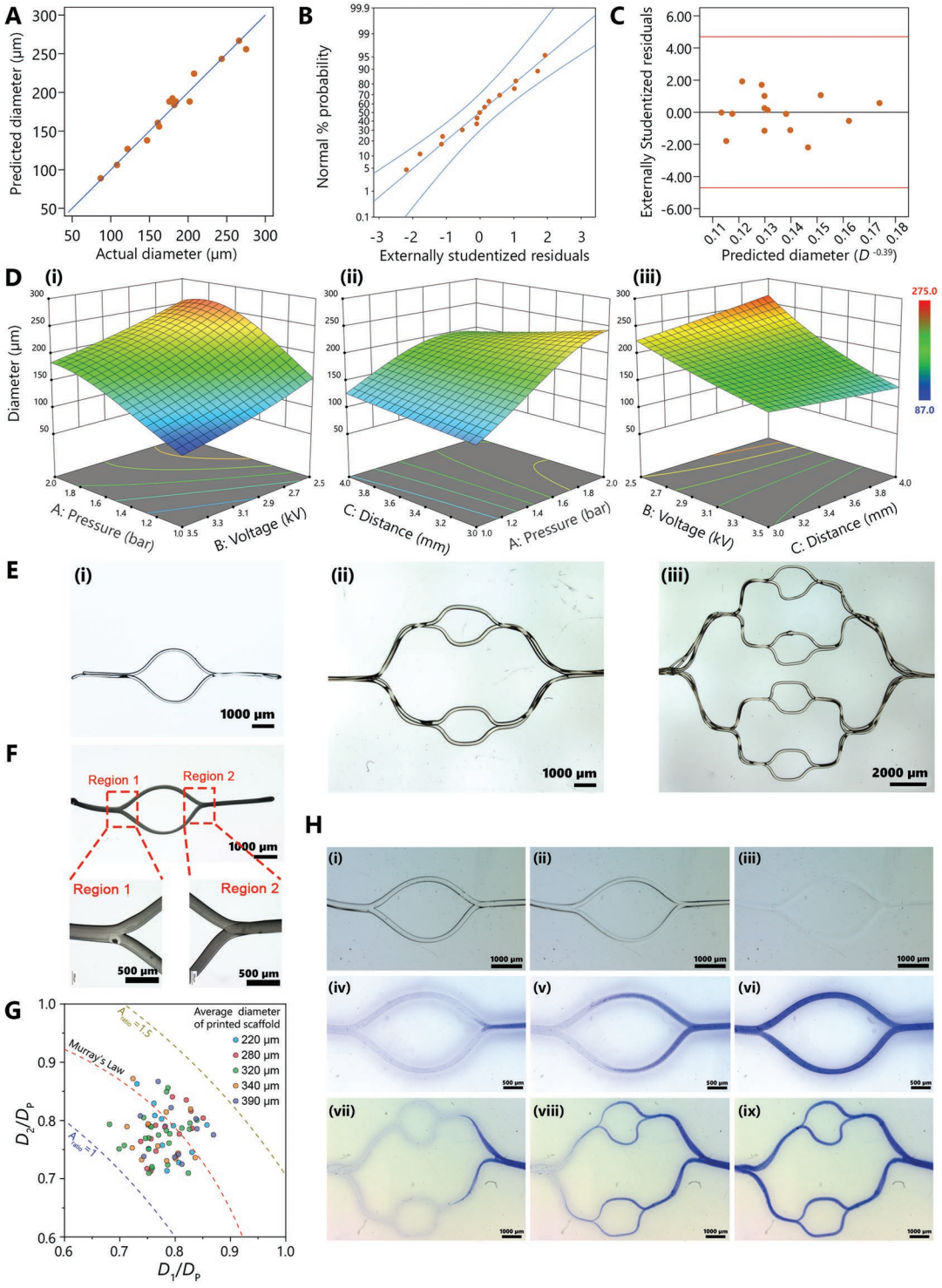

Figure 1. MEW of scaffolds from P*cyclo*PrOx and their behavior in hydrogels. Sanity check for the derived statistical model by RSM to predict the fiber diameter: A) Actual versus predicted fiber diameters from the model; B) the normal plot of residuals (limits of the 95% confidence interval in blue lines); and C) plot of the residuals versus predicted diameter to verify the random distribution of residuals. D) The response surfaces (i–iii) of binary combinations of MEW process parameters, showing the dependency of fiber diameter on model parameters. E) Examples of one (i) and multiple (ii,iii) steps of bifurcation in scaffolds as printed (in dry state before the fusion step). F) Behavior of P*cyclo*PrOx -Scaffolds in GelMA hydrogel matrix: upon immersion in the hydrogel precursor, the fibers swell, leading to the fusion of adjacent fibers (water-induced plasticity). The hydrogel precursors simultaneously evolve into a hydrogel network through crosslinking, resulting in the spontaneous formation of natural bifurcation structures. G) The correlation between parent and daughter vessel diameters with different initial dimensions of fugitive scaffolds. H) Time-lapse images of dissolution of P*cyclo*PrOx after temperature reduction below the LCST (i–iii), and perfusion of interconnected channel system with one (iv–vi), and two (vii–ix) levels of branching.

Swelling of P*cyclo*PrOx resulted in creating microchannels with larger diameters than the templating fibers, with the swelling ratio ranging from 1.3 to 1.5 depending on the initial fiber diameter (Figure S9, Supporting Information). The perfusion of formed structures with a dye (Coomassie blue) revealed that the channels and bifurcations remain interconnected (Figure 1H and Videos S4–S6, Supporting Information), even in more complex geometries.

2.2. Production of Bioreactors Adapted to Perfusable Construct

In order to enable the perfusion of the formed channel networks for cell culture and further microscopy studies, a specialized bioreactor system to host the templating P*cyclo*PrOx scaffolds was developed (**Figure 2**A). Due to the high glass transition temperature (T_g) of P*cyclo*PrOx, the scaffolds could easily be stored in room conditions without the sagging of any overhung structures. Saddle-shaped fixation supports for the scaffolds were created in the main chamber, where the scaffold's inflow and outflow can be placed and precisely positioned (Figure 2B). A drop of concentrated P*cyclo*PrOx solution in water was used as the adhesive to fix the position of the scaffold (Figure 2B). In addition to fixing the position of the scaffold, the adhesive temporarily blocks the in- and outflow to the fluid reservoir and the hydrogel chamber. This prevents blockage of the in- and outlet after introducing hydrogel precursors, and since the adhesive is based on the same material as the scaffold, it can be dissolved and removed by the same stimulus (temperature reduction). The cell culture media could be passively perfused from the integrated fluid reservoirs into the main chamber via rocking on a programmable rocker device. The observation window at the bottom of the main chamber enables microscopy during and after endothelialization. The fixation protocol to integrate sacrificial scaffolds within the bioreactor efficiently preserves the patency of the in- and outlet of created microchannels after forming the hydrogel matrix. Spatial visualization of the course of the microchannel inside the bioreactor was performed using computed tomography (CT) imaging and is shown in Figure 2C,D. Confinement of the contrast agent within the microchannel clearly demonstrates the leakage-free formation of patent microchannels (Video S7, Supporting Information).

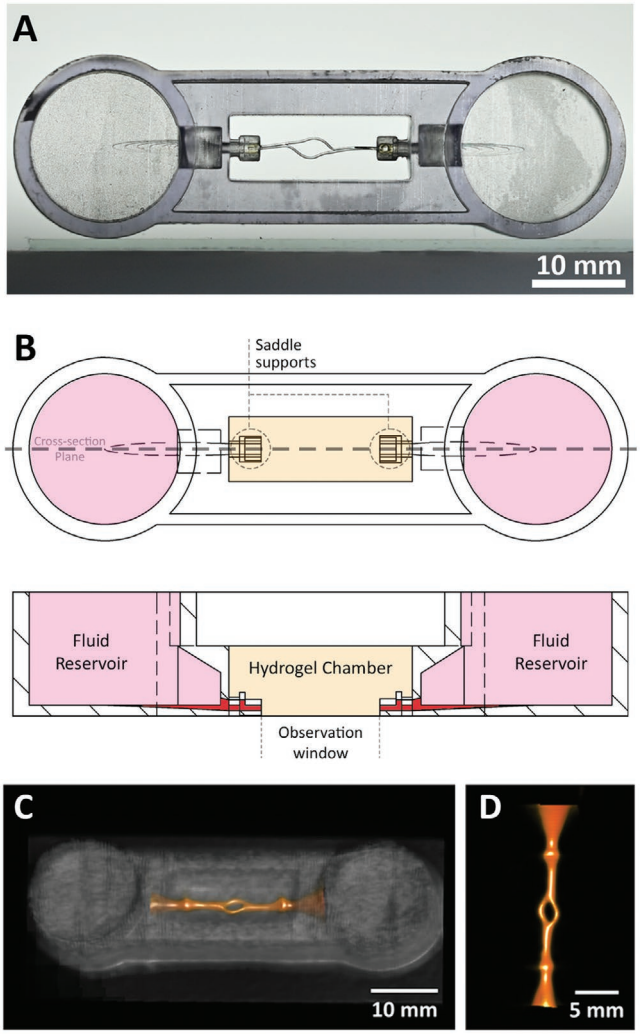

Figure 2. Design of the bioreactor to host and integrate the microchannels created by sacrificial templating of the scaffolds. A) Top-view photo of a bioreactor with P*cyclo*PrOx scaffold embedded on the supporting saddles. B) Design aspects of the bioreactor showing the different components (top) and a cross-section of the top view (bottom). Computed tomography scan of an embedded microchannel: C) image showing the tight and leakage-free connection of microchannel and inlet/outlet of bioreactor. D) Isolated geometry of flow path shown by the contrast agent filling the channel.

2.3. Endothelialization of Microchannels

Primary human umbilical vein endothelial cells (ECs) were used for the biological characterization of the generated system. After dissolution and removing the sacrificial scaffold embedded in the hydrogel matrix, the resulting channels were filled with a suspension of ECs by direct injection, and samples were left at static conditions for 30 min to support cell attachment to the lumen. Perfusion was subsequently applied by placing the bioreactors on the rocker, and cell proliferation was monitored by microscopy (Figure S10A,B, Supporting Information). A fully confluent endothelial monolayer on the lumen of microchannels was formed on day 3 (Figure S10B,C and Video S8, Supporting Information). Cell attachment was stable for at least two weeks after reaching confluency. In parallel, perfusion cell seeding was also performed for comparison. For this purpose, the suspension of ECs was introduced via fluid reservoirs, and bioreactors were directly placed on the rocker system without the 30 min period for the initial attachment. In this experimental setup, cell attachment on the lumen's surface after 24 h was scarce (Figure S10D,E, Supporting Information), indicating the importance of the static attachment phase for the subsequent formation of a stable endothelial monolayer in our model.

Following the bright-field microscopy evaluation (Figure S10, Supporting Information), cell nuclei, endothelial cell marker CD31, and F-actin filaments of endothelial monolayer were stained and evaluated using different microscopy techniques to monitor the cell morphology and attachment to the lumen

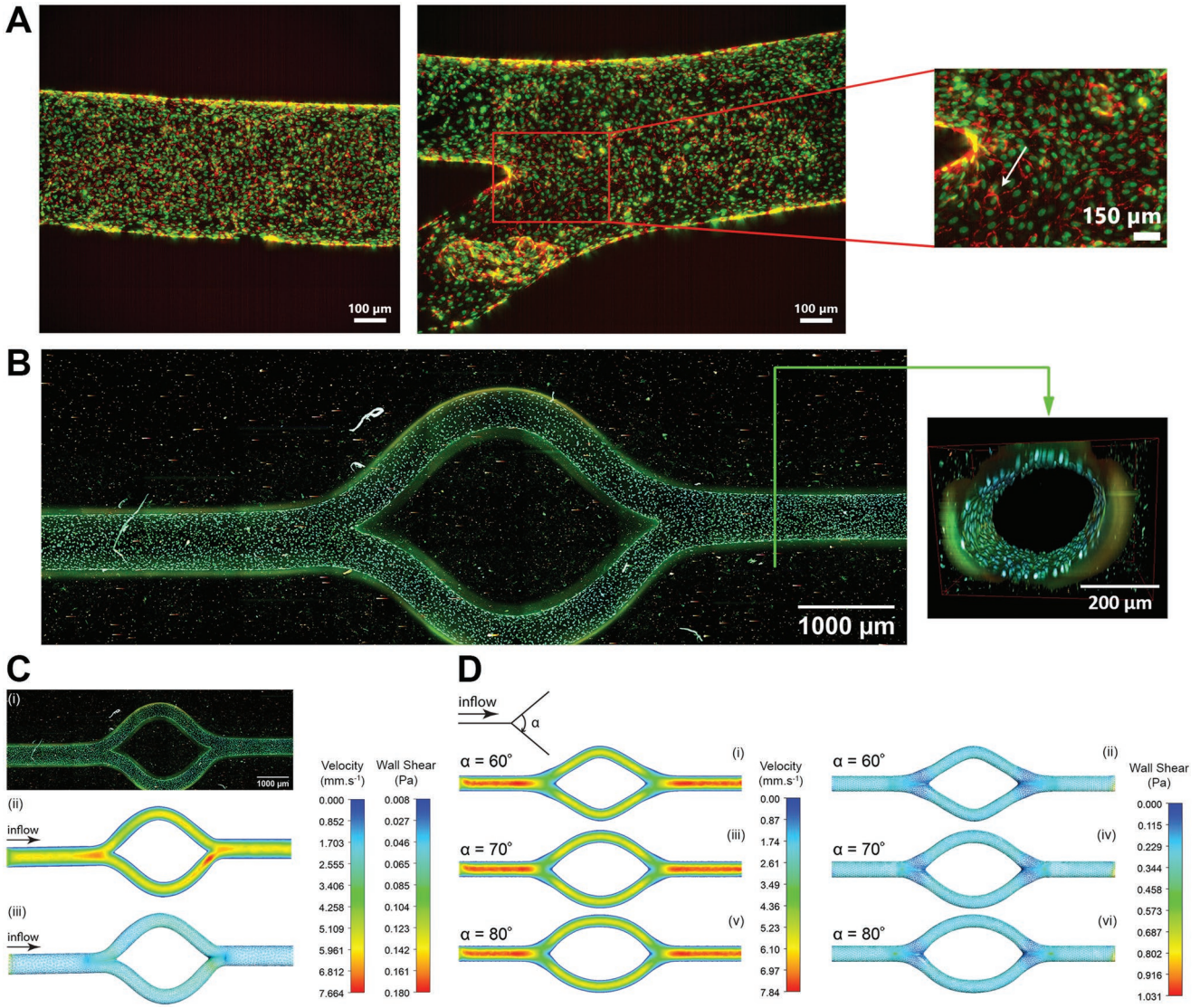

Figure 3. Characterization of endothelialized micronetworks. A) 3D images of the CD31 positive endothelial monolayer on microchannel lumen (magnification 10×, scale bar: 100 µm). Nuclei were stained with Sytox Green and CD31 was visualized with Alexa Fluor 647-conjugated goat anti-rabbit antibody. The white arrow indicates the cell–cell contact with strong CD31 expression. B) Multiphoton imaging of a complete microchannel with endothelial layer: cytoskeleton stained with Alexa Fluor 488 Phalloidin and nuclei stained with Hoechst 33342, the green arrow indicates the 3D cross-section views of marked area. C) Numerical analysis of flow in embedded microvessels. Flow profile and the induced wall shear stress for perfusion of cell culture media in a 3D constructed model based on the geometrical features of endothelialized sample presented in (B). The 3D model was based on data extracted using multiphoton microscopy images. D) Flow profiles and induced wall shear stress calculated for the perfusion of blood in parametrized 3D design of microchannels with different bifurcation angles.

surface in 3D as well as the lumen's circularity. 3D Thunder imaging showed the presence of endothelial monolayer and good cell–cell contacts on the lumen surface (**Figure 3**A). Confocal microscopy images confirmed a uniform cell attachment to the lumen surface with a large cell number after 3 days post-seeding (Figure S11, Supporting Information). Furthermore, by using multiphoton microscopy, it was possible to visualize the 3D structure of the entire lumen of the channels and the branches (Figure 3B and Figures S12 and S13, Supporting Information). Additionally, a 3D reconstruction of the confluent ECs monolayer coating the inner lumen of the channel is provided in Video S9, Supporting Information.

2.4. Numerical Analysis of Flow within the Embedded Microchannels

A numerical flow simulation of the cell culture medium through the bifurcated channels was performed based on the 3D reconstruction of an endothelialized microchannel (Figure 3C). The expansion ratio above one resulted in decreased velocity of medium passing through the daughter branches, although minor irregularities in the generated computer-aided design (CAD) model resulted in a slight increase in velocity at the outlet of one of the branching segments. However, this increase did not affect wall shear stress significantly,

as the simulated value of flow-induced wall shear stress was generally minimal (0.05 Pa), except for the beginning and end of the bifurcating regions, where it reached ≈0.1 Pa (1 dyn cm^{-2}) which was due to the lack of smoothness in the generated 3D model. It should be noted that because of the simplifications made for the boundary conditions in numerical simulations, the outlet region was set to be at atmospheric pressure. This contributed to the absence of any back pressure within each perfusion half-cycle and, consequently, the slight overestimation of the outlet's flow velocity.

The influence of bifurcation angle on three different microchannels' designs was analyzed using a numerical simulation of blood flow through the channels with different bifurcation parameters (Figure 3D). The comparison between different induced flow profiles showed that blood velocity at fixed Ht of 0.45 flowing within microchannels in parent and daughter vessels was not significantly altered by increasing the bifurcation angle. The same was observed for the wall shear stress, where the daughter branches in all models experienced a similar wall shear stress of ≈0.22 Pa, independent of the bifurcation angle. The calculated flow profiles showed that the blood velocity within the daughter branches decreased compared to those of parents, indicating a unique biomimetic design due to the volumetric redistribution of plasticized sacrificial scaffolds at the later stage of the print-and-fuse methodology.

2.5. Endothelial Barrier Function and Response to Stimuli

To investigate the permeability of the endothelial layer, two different sizes of fluorescein isothiocyanate (FITC)-labelled dextran, 20 and 200 kDa, were used. Dextran solutions were perfused directly through the inlet into the microchannels with and without ECs monolayer and imaged by fluorescence microscopy at the onset of dextran injection and 2 h later to visualize the dextran diffusion into the hydrogel matrix (**Figure 4**A). The fluorescence intensity inside the microchannel and in the surrounding hydrogel was measured to evaluate the barrier function provided by the endothelium compared to non-endothelialized channels. The presence of the endothelial layer strongly reduced the diffusion from the channels into the hydrogel matrix for both dextran sizes (Figure 4B). Immediately upon the injection (Figure 4C), no significant difference in 20 kDa FITC–dextran diffusion was observed between non-endothelialized and endothelialized channels. However, after 2 h, the diffusion of 20 kDa FITC–dextran into the hydrogel matrix was reduced by 25% in the presence of the ECs monolayer. As expected, the diffusion of 200 kDa FITC–dextran into the hydrogel was overall strongly reduced as compared to 20 kDa FITC–dextran due to the larger size of the molecules (Figure 4B). Here, the difference between non-endothelialized and endothelialized channels was even more pronounced, as shown by the different slopes of the lines in Figure 4D. Immediately after the dextran injection, 30% less diffusion into the surrounding hydrogel was observed in endothelialized channels compared to non-endothelialized ones. Moreover, the diffusion rate of dextran in non-endothelialized samples was comparable, slightly faster for 20 kDa FITC–dextran than 200 kDa molecules, due to the smaller size of the molecules. In contrast, the diffusion in endothelialized samples was reduced by nearly a half after 2 h compared to non-endothelialized ones, indicating that the organization of the endothelial layer inside the microchannels was sufficient to mimic the barrier function of blood vessels.

To test whether endothelial cells seeded inside the microchannels maintain their function and responsiveness to inflammatory stimuli, the cells were stimulated with tumor necrosis factor (TNF)-α under static or perfused conditions. Our previous studies showed that bifurcating Ibidi slides represent a suitable in vitro model to study the effects of wall shear stress on endothelial response to inflammatory cytokines.[23,24] Therefore, we used ECs seeded in Ibidi slides as an experimental 2D control. EC activation by TNF-α was monitored in both systems in parallel to compare the upregulation of endothelial adhesion molecules, VCAM-1 (vascular cell adhesion molecule 1) and E-selectin, in 2D and 3D. The imaging of adhesion molecule expression was performed using different techniques, namely, fluorescence microscopy for Ibidi slides and confocal microscopy for microchannels. The results showed that TNF-α stimulation resulted in upregulation of VCAM-1 and E-selectin, both in 2D and 3D samples (**Figure 5**). In control samples without TNF-α stimulation, there was no recognizable expression of the adhesion molecules (data not shown). In samples stimulated with TNF-α under perfused conditions, the expression of perinuclear VCAM-1 was reduced compared with the static samples (Figure 5A). This effect was previously observed in 2D Ibidi slides and was now confirmed in the 3D endothelialized microchannels. Similarly, overall upregulation of E-selectin molecule was less pronounced in perfused samples than in static conditions for both 2D channels and 3D microchannels, although the effect was not statistically significant in 2D samples (Figure 5B). The quantification of the perinuclear expression of E-selectin showed slightly higher values in static conditions than in perfused systems for both Ibidi slides and the microchannels.

3. Discussion

This study presents an integral approach to fabricate 3D bulk-hydrogels with embedded biomimetically branched microvasculature inside a perfusable bioreactor system. It comprises the print-and-fuse approach to generate sacrificial templates for the microchannels that can be tuned regarding the channel diameter, with a good approximation of Murray's law to estimate the parent channel diameter based on the daughter vessels. The integration of these scaffolds with flexible design within a customized bioreactor ensures the perfusability of the final construct. This system allows a broad range of flexibility and freedom regarding the choice of hydrogels to cast into the bioreactor.

Optimized by RSM, it was possible to fabricate sacrificial templates using MEW to form a naturally branching and interconnected microchannel network in hydrogels. During the past years, demand to form intricate and interconnected networks mimicking the vascular system led to developing various sacrificial templating methods. The wider accessibility, a larger user community, and technological simplicity contributed to

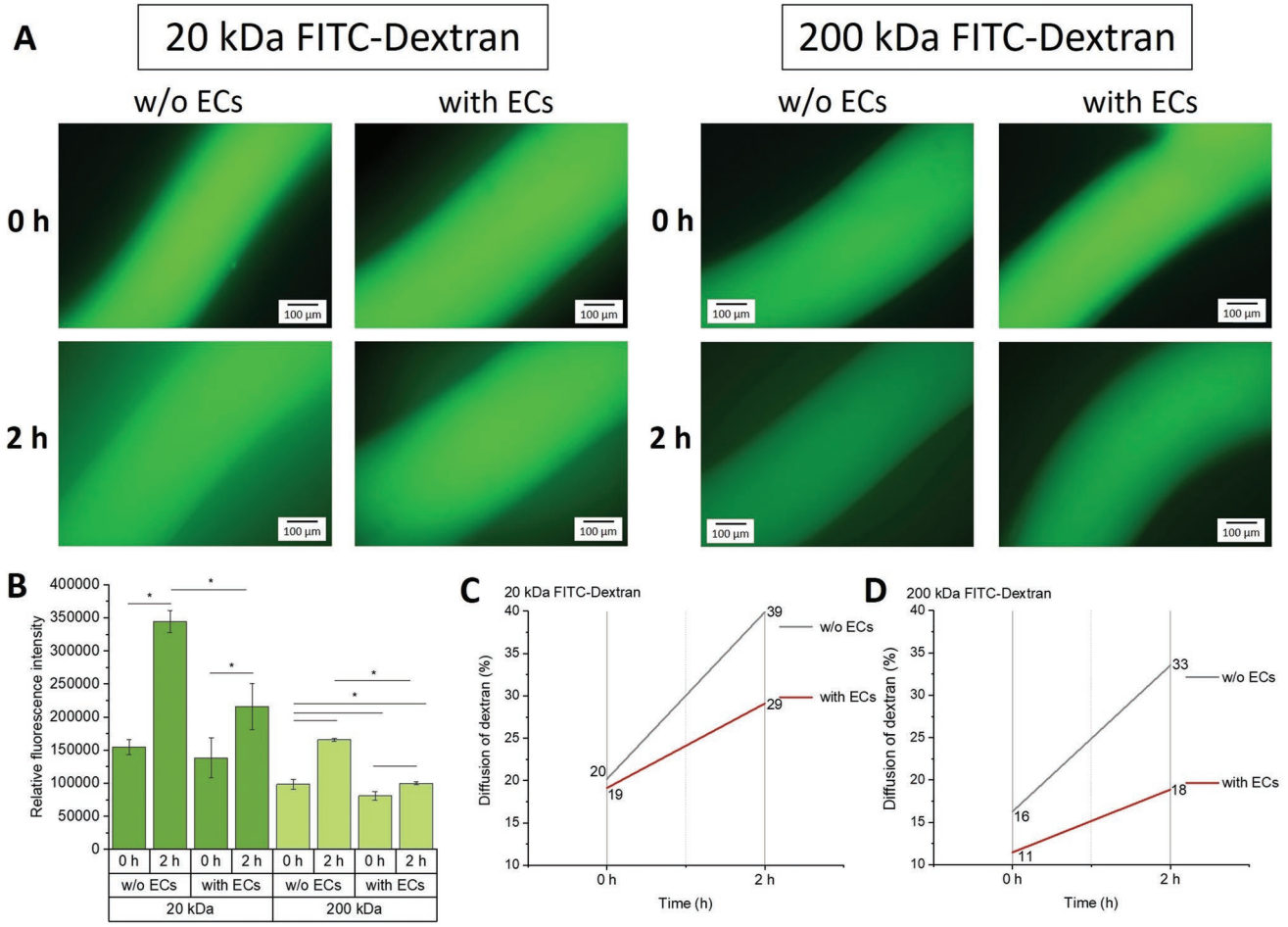

Figure 4. Channel permeability to fluorescently labeled dextrans. A) Fluorescence images at 0 and 2 h after perfusion of FITC–dextran in microchannels. Left panel: 20 kDa FITC–dextran; right panel: 200 kDa FITC–dextran. B) Comparison of the diffusion rate between microchannels with and without endothelial monolayer: fluorescence intensity of dextran molecules diffused into the hydrogel. C,D) Percentage calculation of the diffusion for the respective dextran. $*p < 0.05$.

the popularity of extrusion-based (bio)printing for sacrificial templating. Nevertheless, limitations in the resolution of the process and the spatial considerations in the fabrication of 3D structures are two challenging factors in realizing microvascular systems by this method. Compared to conventional 3D extrusion printing, MEW provides the possibility to deposit fibers in micrometer size.[26] Moreover, by introducing the commercial bioprinters with MEW-enabled modules or standalone MEW printers, MEW technology is on its way to being as accessible as conventional extrusion printing. High resolution in the production of sacrificial structures[25] and tunability of the process in fabricating a wide range of dimensions are two essential advantages of MEW.

Production of low-dimension templates by MEW is especially interesting, as achieving high resolution is a critical challenge for the other methods of channel creation. Fabrication of geometrically consistent microchannels is essential in ensuring the uniform distribution of nutrients and oxygen in a large hydrogel structure. The optimization capacity of MEW through DoE adds to the flexibility of the templating design, and depending on the dimension requirements, it is possible to create predictable and defined architectures with this method.

Biocompatible templating of microchannels is mainly performed using thermoresponsive sacrificial inks[12–14,27] or water-soluble carbohydrate-based structures.[17,18] Pioneered by the group of J. Lewis, extensive studies on vascularization by sacrificial inks such as pluronics or gelatin have been performed.[12–14,27] These methods could achieve a significant level of geometrical complexities. However, critical bottlenecks include some design aspects, such as the microchannels' circularity and creating overhang branching sacrificial structures. Additionally, microchannels created by carbohydrate-based templates need post-fabrication stabilization by dip-[17] or spray-coating[18] methods to control the fast dissolution rate in hydrogel matrices, resulting in complexities in the fabrication process and the formation of a barrier between endothelium and tissue.

As an alternative to current sacrificial materials, we used thermoresponsive P*cyclo*PrOx because of its intrinsic biocompatibility,[28] its LCST within the physiological range[29] at 25 °C, and its unique water-induced plasticity. P*cyclo*PrOx fugitive

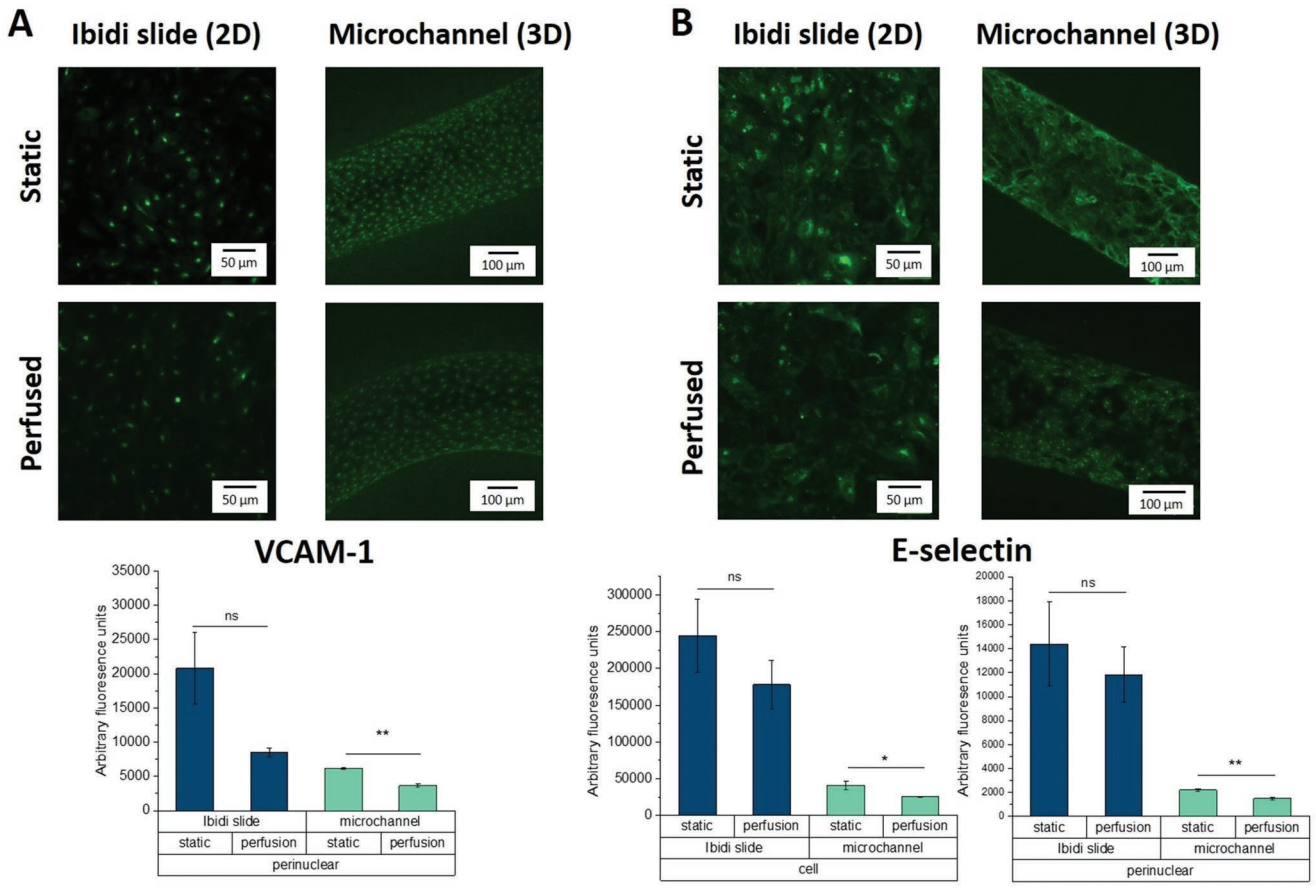

Figure 5. Endothelial response to stimuli. A) Top: representative fluorescence (Ibidi slides) and confocal images (microchannels) show perinuclear upregulation of VCAM-1 in TNF-α-treated ECs; Magnification 20×. Bottom: data quantification. The graph shows the TNF-α-induced VCAM-1 expression determined by immunofluorescence staining. ** $p < 0.005$; *$p < 0.001$; ns: not significant. B) Top: representative fluorescence (Ibidi slides) and confocal images (microchannels) show cytoplasmic and perinuclear upregulation of E-selectin in TNF-α-treated ECs; Magnification 20×. Bottom: data quantification. Graphs show the TNF-α-induced E-selectin expression (total and perinuclear) determined by immunofluorescence staining. ** $p < 0.005$; *$p < 0.001$; ns: not significant.

scaffolds show progressive plasticity in contact with water below the glass transition temperature. However, the rate of this behavior is slow enough to enable casting of the hydrogel precursors without loss of scaffold's integrity, and at the same time, quick enough to result in the fusion of adjacent fibers and formation of biomimetic branching structures during the gelation of hydrogel matrix. Nevertheless, P*cyclo*PrOx shows low hygroscopicity and sensitivity to the temperature at room conditions. These properties practically extend the applicability of P*cyclo*PrOx sacrificial scaffolds compared with the traditional fugitive materials, as the latter demand special storage and handling procedures[16–18] or should be manufactured just prior to embedding in the hydrogel matrix.[12,13] P*cyclo*PrOx structures can be quickly dissolved and removed by cooling to slightly below room temperature. This provides a more convenient and cell-friendly process than other fugitive inks with LCST behavior, such as pluronics. Additionally, the distinctive feature of P*cyclo*PrOx sacrificial structures is the water-induced plasticity, a property that results in the fusion and merging of adjacent microfibers in contact with water without significant loss in shape fidelity.

Conventionally, fugitive inks such as Pluronics show an excellent recovery after the extrusion, enabling the creation of singular channels with high fidelity; however, the high elasticity results in the poor merging or fusion of adjacent or overlapping strands. This behavior contributes to creating generally overlooked geometrical inaccuracies such as grooving. Other fugitive inks such as gelatin show improved smoothness and merging behavior in branchings,[13] although shape fidelity is impacted. The print-and-fuse strategy demonstrated in this study relies on a combination of plasticity of adjacent P*cyclo*PrOx fibers, confined by the evolving elasticity of the hydrogel matrix undergoing crosslinking. A direct result of this structural development is the formation of smoothed branchings with a good degree of circularity of the lumens and in good agreement with Murray's law, independent of the size of the initial fibers. To explain why such dynamics of fusing and arrangement of filaments embedded in hydrogel matrix were observed, we considered the principle of minimum work in Murray's law, which, in its general form, describes the balance and tradeoff between the energy needed to transport a mass through the microvessels and the energy needed to

maintain the mass within.[30] Assuming that such correlation applies to the systems in which the viscosity only depends on the shear,[31] the driving force to form branching structures in this study could follow the same principles and be based on the balance between residual pressure due to swelling, surface energy at the interface, and the viscosity of the plasticized P*cyclo*PrOx confined by a hydrogel matrix. In vivo, the correlation between the diameter of parent and daughter vessels in the vascular system is such that the combined cross-section areas of daughter vessels is greater than that of the parent's.[32] The measured diameters of microchannels created in this study were above the expansion ratio of 1.0, indicating that merging the P*cyclo*PrOx microfibers resulted in a mass flow during the fusion process. This effect was independent of the initial diameter of fugitive scaffolds. Combining this mass flow with the smooth merging of the microfibers resulted in branching microchannels approaching the two requirements of minimum wall material and constant wall stress for microvessels.[33]

Integration of (micro)channels created by sacrificial templating into a perfusion system is a critical step that, if performed poorly, could potentially attenuate the intended functionality of the design. Traditionally, sacrificial templates and the perfusion apparatus are considered the two separate components of the artificial vascularized system. To enable perfusion, a common practice is to create in- and outflow paths during post-processing. In this way, through holes within fully crosslinked hydrogel matrices enclosing the sacrificial structures are usually created with the aid of (micro)needles. This procedure is susceptible to errors, especially in the case of micron-scale channels. Failure at this stage would damage the hydrogel matrix, causing leakage during perfusion and even loss of functionality. The methodology presented in this study wholly eliminates the errors caused by mishandling at the post-processing stage in conventional designs. The integrated design of sacrificial scaffolds within the perfusion chamber provides the opportunity to seal the in- and outflow regions of the hydrogel body prior to the addition of the pre-gel. Moreover, the application of P*cyclo*PrOx as the adhesive for sealing the fluidic path creates a homogeneous and conformal connection between the fluid reservoir and microchannels. Upon triggering the thermal stimulus, both the microchannel and the adhesive are removed quickly, creating a one-step process to fabricate an open microchannel system connected to fluid reservoirs. The precise positioning and fixation of sacrificial scaffolds is an essential part of the presented design, which could enable the customization of the flow path depending on the specific needs through the arrangement of the support saddles. Thus, although the pre-fabrication of the sacrificial structure requires more steps than, for example, direct printing in a bioreactor, this approach has a number of advantages: First of all, the printing can be done without outer spatial restrictions on a flat substrate. The structures can be printed in a size and geometry that perfectly fits the bioreactor inlet and outlet, so that upon filling with gel, the channel is surrounded in three dimensions, without contact with any internal surface of the bioreactor. Moreover, the pick-and-place positioning of the sacrificial structure in the bioreactor is straightforward and easily done with a tweezer. Hence, the bioreactor design not only guarantees leakage-free perfusion, but in addition permits rapid assembly in labs where no printer is available. This decoupling of printing and assembly steps is therefore not only robust and reproducible, but it also allows virtually any biology lab to use this approach in combination with a large variety of biomaterial inks or bioinks.

Lack of vascular network may limit oxygen diffusion in thicker biofabricated constructs and cause cell death due to hypoxia. However, the microvasculature in vivo is more than a passive network of channels allowing the supply of oxygen and nutrients or removing metabolic byproducts. Its role in tissue function and orchestrating the response to hemodynamic and metabolic stimuli largely depend on vascular endothelium.[34,35] For the biological characterization of the generated system, we therefore used primary ECs. The endothelialization was performed by short-term static cell seeding to allow initial cell attachment, followed by fluid perfusion. Using this method, it was possible to achieve a confluent endothelial monolayer lining the inner part of the microchannel in three days.

In vivo, endothelium serves as an interface between blood and tissue, providing a semipermeable barrier that controls the exchange of molecules.[34,35] A functional endothelial barrier restricts the passage of macromolecules larger than 60–70 kDa.[36,37] On the other hand, increased permeability to macromolecules as large as 2000 kDa across endothelial monolayers may occur depending on external stimuli that result in destabilization of the endothelial cytoskeleton, degradation of the glycocalyx, or disruption of cadherin-mediated cell–cell contacts.[37] In order to test the barrier function of endothelium lining our microchannels, we assessed the diffusion of fluorescently labeled dextrans from the channels into the surrounding hydrogels. Our results showed that the presence of endothelium significantly inhibited the passage of dextrans, both at low and high molecular weights, as compared with non-endothelialized channels. This indicates that the barrier function of endothelial cells lining at the inner surfaces of the microchannels is preserved and effective. It must be noted that monolayers of cultured endothelial cells are usually 10 to 100 times more permeable to macromolecules than the endothelia of microvascular walls.[36] However, although microvascular endothelium acts as a barrier to large molecules, it is not an absolute barrier even in vivo.[38] Therefore, despite this limitation, our model can serve investigations of macromolecular transport across endothelium and intracellular processes associated with changes in endothelial permeability.

The endothelium is not a passive barrier between blood and tissues, but is actively involved in hemostasis and inflammatory responses, besides fluid and solute exchange.[35,39] ECs respond to pro-inflammatory cytokine TNF-α with a rapid expression of cell adhesion molecules,[40,41] including E-selectin and VCAM-1, which are de novo synthesized within 30–120 min of TNF-α stimulation[42] and transported to the endothelial surface. Our present results showed that TNF-α stimulation resulted in upregulation of VCAM-1 and E-selectin in ECs lining the lumen of the 3D channels, confirming that these cells maintain their function and responsiveness to inflammatory stimuli.

In vivo, the signaling pathways activated by laminar shear stress prevent inflammatory response in the vessels exposed to TNF-α.[40] We therefore compared the effects of TNF-α stimulation in our models exposed to static or perfused conditions.

Although the used rocking system does not provide the typical unidirectional flow as present in the circulation, the reduction in the adhesion molecules expression was observed under perfused conditions. To gain an understanding of the flow conditions prevailing in the 3D bifurcating microchannels exposed to perfusion by rocking, a numerical flow analysis was performed. The results showed that the small diameter of microchannels in this study with no active pressure during cycling resulted in slower flow velocity within the microvessels in different regions (≈0.33 cm s^{-1}, with a maximum value of 0.78 cm s^{-1}) as compared to the data measured in vivo. As an example, in human finger vessels with diameters of 800 µm to 1.8 mm, arterial blood flow velocities ranging from 4.9–19 cm s^{-1} and venous blood flow velocities at 1.5–7.1 cm s^{-1} were reported.[43] In smaller human cortical venules (below 20 µm), time-averaged flow velocity was 0.5 cm s^{-1} in non-pulsatile veins and 1.1 cm s^{-1} in pulsatile veins.[44] The average wall shear stress in different regions during each rocking half-cycle was also significantly below the values reported for the small arteries and veins,[45] which is mainly associated with relatively slow perfusion velocities and also operation in atmospheric pressure. Despite these differences in flow velocities and wall shear stress, we noted the protective effect of perfusion on the ECs exposed to TNF-α stimulation, both in 2D and 3D conditions. Therefore, the slow bi-directional flow used in the present experimental setup can, to some extent, mimic the beneficial effect of laminar flow in the vasculature. Considering the unique biomimetic characteristics of this model and its straightforward assembly, the print-and-fuse methodology promises a much broader use of vascularized 3D tissue models in the biological community, where the need for such methods is dramatically growing.

4. Conclusions

This study introduces an integrative and facile approach for the reproducible generation of perfusable and functionally endothelialized microvascular networks within bulk hydrogels. The described method based on thermoresponsive P*cyclo*PrOx scaffolds produced by MEW allows for the precise fabrication of sacrificially templated microchannels with good control over the dimensions within a hydrogel matrix. A specifically useful feature of the system is the high degree of freedom concerning the choice of hydrogel system, which makes it broadly applicable to a range of commonly used hydrogel formulations with specific biochemical features. Furthermore, the print-and-fuse approach described here allows the generation of biomimetic bifurcations in a wide range of diameters and complexities. By the integrative design of the bioreactors tailored to the scaffold dimensions and characteristics, perfusable and interconnected channel networks are easily created, ready for subsequent endothelialization and microscopic assessments. By providing a functional endothelial monolayer, our model can serve as a tool to investigate cell activation and signal transduction, macromolecular or drug transport, and intracellular processes associated with changes in endothelial permeability.

The advantages of the presented design for creating microvascular networks include precise, reproducible and adaptable biomimetic channel diameters and designs, facile removal of sacrificial structures, the flexibility regarding the choice of hydrogel matrix, as well as rapid functional endothelialization. Those advantages thus make our print-and-fuse approach, which addresses some of the limitations of the current methods for creating microvascular constructs, a broadly applicable alternative platform for the generation of vascularized tissue models.

5. Experimental Section

Synthesis of PcycloPrOx: The monomer and the polymer were synthesized and characterized according to literature (see Supporting Information for a detailed description).[29]

Melt Electrowriting: An in-house developed MEW printer was used to produce sacrificial scaffolds, and the related details are described elsewhere.[19] In order to produce homogenous fibers, the polymer reservoir in the MEW printer was equipped with two heating zones, one at the syringe body and another at the nozzle. Different temperature profiles for MEW of P*cyclo*PrOx are listed in **Table 1**. A heated collector plate connected to a temperature controller (C448, Hotset, Germany) was used to enable precise control over fiber deposition. The G-code used to print the sacrificial scaffolds is described in the Supporting Information.

Design of Experiments for Prediction of Fiber Diameter: RSM was used to investigate the individual and interaction effects of MEW process parameters on the resultant P*cyclo*PrOx diameter. Three process parameters at three levels were chosen to construct the DoE based on a Box-Behnken design with 3 center points using Design-Expert software (version 13, Stat-Ease, Inc., Minneapolis, MN, USA). The details of the parameters and their values are listed in **Table 2**. Fiber diameters were measured using a stereomicroscope (DMS-1000, Leica Microsystems, Germany) on scaffolds printed with one level of bifurcation. The obtained images were quantified using Fiji.[46] The final diameter value for each run was based on the average value of diameter obtained from at least 150 measurements on 15 different scaffolds, randomly chosen from a pool of 30 generated with the same experimental conditions. A polynomial equation was used to fit the experimental data, and it was evaluated by analysis of variance (ANOVA) and coefficient of determination (R^2). The significant parameters were determined using *F*-value by calculating $F_{critical}$ and *p*-value with $\alpha = 0.05$. A power model transformation was used to find the best fit. The obtained model was validated by producing 3 sets of different one-level bifurcated scaffolds, with MEW parameters chosen randomly within the experimental range.

Design and Fabrication of Perfusion Bioreactor: A CAD model of the perfusion chambers was created using Solidworks 2018 (Dassault Systemes, Vélizy-Villacoublay, France). An Autodesk Ember digital light processing (DLP) 3D printer with Autodesk Print Studio slicer (Autodesk, San Rafael, USA) was used to fabricate the designed bioreactors. A FotoDent guide 405 nm (Dreve Dentamid GmbH, Unna, Germany) was used as the photopolymer resin.

Creation of Microchannels within Bioreactors: Sacrificial P*cyclo*PrOx scaffolds were placed on the saddle supports of the bioreactors, fixed on their position using 1:1 dilution of 30 wt%/v P*cyclo*PrOx in MilliQ solution. After drying the adhesive at room temperature, glass coverslips with the standard dimension of 25 × 60 mm were attached to the bottom part of the bioreactor using a fast-setting silicone resin (Dublisil 15, Dvreve, Germany). After setting the resin, bioreactors with sacrificial scaffolds were sterilized under UVC light for 15 min. GelMA

Table 1. Temperature (T.) profiles for MEW of P*cyclo*PrOx.

Material	T. syringe [°C]	T. nozzle [°C]	T. collector plate [°C]
P*cyclo*PrOx	210	225	70

Table 2. Parameters and their corresponding ranges (coded and actual values) for the creation of different runs of the DoE.

Parameters	Coded	Coded levels (actual values)		
Pressure [bar]	P	–1 (1)	0 (1.5)	+1 (2)
Voltage [kV]	V	–1 (2.5)	0 (3.0)	+1 (3.5)
Distance [mm]	H	–1 (3.0)	0 (3.5)	+1 (4.0)

(gel strength 300 g Bloom, 80% degree of substitution, Sigma-Aldrich, Munich, Germany) was dissolved in cell culture media at 7% final concentration at 37 °C. Lithium-phenyl-2,4,6-trimethylbenzoylphosphinat (LAP) was used as the photoinitiator. A 0.5 wt%/v stock solution of LAP in PBS was prepared and stored at 4 °C, and a final concentration of 0.05 wt%/v was used to crosslink the GelMA hydrogel. Hydrogel precursors to prepare 400 µL of final hydrogel were inserted into the main chamber of the bioreactor and crosslinked by a UVA light source (Vilber Lourmat, Marne-la-Vallée, France) for 8 min. Once crosslinking was completed, PBS solution was added to the bioreactor chambers to dissolve the sacrificial scaffold, and if demanded, bioreactors were placed shortly on ice to reduce the dissolution time.

Computed Tomography: A C-arm cone-beam CT scanner (Siemens Artis zee floor, Siemens Healthcare, Forchheim, Germany) was used for the 3D visualization of the vessels. Following the studies on optimal dosing and dilution of the contrast agent, an 8-second digital subtraction angiography H-run with a tube voltage adjusted to 55 kV was performed to obtain the 3D sequences. After recording the native sequence, 5 mL of a sodium iodide solution of 100 mg mL^{-1} was injected into the channel for the contrast-enhanced sequence. The 3D reconstruction of chambers and microchannels was done with a voxel edge length of 0.18 mm. The software MultiModality Workplace (Siemens Healthcare) was used to process the 3D volume data. This technique allowed spatial visualization of the course of the microchannel inside the bioreactor. The movie recording was done with Camtasia Studio software (TechSmith, Okemos, MI, USA).

Computational Flow Analysis: The reconstruction of the 3D models was performed in Solidworks software (Dassault Systèmes, Vélizy-Villacoublay, France). The 3D model of the real geometry was produced based on the 3D mosaic stacks of the whole endothelialized microchannels acquired using multiphoton microscopy. The parent and daughter sections of bifurcated microvessels were generated by a controlled loft function of an ellipse cross-section with the ratio of the diameters of 4:3.1 along the degree 9 Bezier curves. The apex radius of the bifurcation zones was extracted from the microscopy images. The 3D models with different bifurcation angles were designed by a parametric approach described elsewhere.[47] For the parent and daughter segments, circular cross-sections with diameters of 500 and 400 microns were considered, respectively.

The flow profile of cell culture media or blood in 3D models of bifurcated microchannels was computed using Ansys Fluent (Ansys, Canonsburg, PA, USA). The inlet mass flux was determined based on experimental values. The viscosity and density of the cell culture media were obtained from the data reported by Poon.[48] The in vitro viscosity law developed by Pries et al.[49] at the parent vessel was adopted and implemented for both parent and daughter segments. The hematocrit for the determination of blood viscosity was fixed at 0.45. Both the cell culture media and the adopted blood viscosity profiles were assumed to behave as Newtonian fluids. The influence of gravity on flow during the perfusion was considered in all the computations with atmospheric pressure as boundary condition.

Endothelial Cell Seeding: Primary human umbilical vein endothelial cells (ECs) were isolated from freshly collected umbilical cords by a standard technique.[50] Isolated cells were maintained in an endothelial cell growth medium (Promo Cell, Heidelberg, Germany) with the endothelial cell growth supplement containing 5% fetal calf serum, 4 µL mL^{-1} heparin, 10 ng mL^{-1} epidermal growth factor and 1 µg mL^{-1} hydrocortisone, in a humidified 5% CO_2 incubator. The use of human material was approved by the Ethics Committee of the Faculty of Medicine at the University of Erlangen-Nürnberg (case no. 246-13B). All subjects enrolled in this research have given informed consent according to the ethical guidelines. In all experiments, ECs at passages 1–3 were used.

Microchannels were coated with fibronectin solution at 50 µg mL^{-1} end concentration for 1 h at 37 °C. Channels were washed once with PBS after the coating process. ECs suspension was prepared at 7×10^6 cells in 100 µL of cell culture media, and 10 µL batches were seeded into the channels. After cell seeding, the bioreactors were left under static conditions for 30 min at 37 °C in a humidified CO_2 incubator, and bioreactors were turned upside down after 15 min to enhance the homogeneity of the cell attachment. After 30 min, 750 µL of cell culture media was added to the inlet, and outlet chambers and bioreactors were placed on an interval rocker platform (MIMETAS BV Leiden, Netherlands). For the perfusion cell seeding, 1×10^6 cells per bioreactor were suspended in 1000 µL of cell culture media and applied directly into the inlet and outlet chambers (500 µL volume per side). Immediately afterward, samples were placed on the interval rocker platform. The rocker was set for continuous perfusion at a 10-degree inclination and a 10-min cycle timer. Cell attachment was controlled 24 h post-seeding by light microscopy with Axiovert 40 CFL (Zeiss, Jena, Germany). Microchannels with less than 70% cell coverage underwent a secondary cell seeding at a 48 h time point to achieve a fully confluent endothelial layer on day 3.

Characterization of the Endothelial Layer: To evaluate the density of the endothelial monolayer on the microchannel surface, cell-seeded samples were imaged daily by an inverted microscope, and the endothelialized area was calculated by Fiji[46] software. When a full endothelial monolayer was achieved, cells were stained with fluorescent dyes including Hoechst 33342, Sytox Green, rhodamine phalloidin (Invitrogen, Thermo-Fisher, Schwerte, Germany), and Alexa Fluor 488- conjugated phalloidin (Promokine, Heidelberg, Germany) to visualize the cell nuclei and cytoskeleton. Cells were fixed with 4% buffered paraformaldehyde and permeabilized with 0.2% Triton X-100 in PBS. F-actin filaments of cells were stained either stained with rhodamine phalloidin with the final concentration of 200 units/mL or with Alexa Fluor 488-conjugated phalloidin at 1:100 dilution depending on the microscope type. Nuclei were visualized using Sytox Green at 1:1000 dilution or Hoechst 33342 with the final concentration of 0.5 µM depending on the microscope type. The main reason for choosing different wavelengths of nuclei staining solutions for different microscopes was the laser configuration of the respective devices. Cell morphology was observed using an upright SP5X laser scanning confocal microscope (Leica Microsystems GmbH, Wetzlar, Germany) with a 20×/1.0 NA water immersion objective. Additional staining of cell–cell contacts was performed using an anti-CD31 antibody (monoclonal rabbit anti-human, Clone SP38, dilution 1:50, Sigma-Aldrich) and the secondary Alexa Fluor 647-conjugated goat anti-rabbit antibody (Invitrogen). Stained cells were visualized by Leica Thunder 3D Imager Widefield with 10× dry objective (Leica Microsystems GmbH, Wetzlar, Germany).

The endothelialized channels embedded in hydrogel were subsequently imaged within the bioreactor. An upright multiphoton microscope system (TriMScope II, LaVision BioTec, Bielefeld, Germany) described in ref. [51] was employed. The large overview 3D mosaics of a whole construct were acquired with a Nikon Plan Fluor 10×/0.3NA objective (Nikon Corporation, Tokyo, Japan). Detailed high-resolution image stacks of smaller regions of interest were acquired with a 25×/0.95NA HC FLUOTAR L objective (Leica Microsystems GmbH). Images were recorded using an excitation wavelength of 810 nm and detecting the two-photon fluorescence using 450 (450/70, shown as blue), 525 (525/50, shown as green), and 620 nm (620/60, shown as red) emission filters (Chroma Technology group, Acal BFi Germany GmbH, Dietzenbach, Germany). The full-construct 3D mosaic was acquired with a voxel size of $1 \times 1 \times 1$ µm^3 with a 1.1×1.1 mm^2 field of view of each mosaic piece. The high-resolution image stacks of regions of interest were acquired with a voxel size of $0.4 \times 0.4 \times 1$ µm^3 in a 0.4×0.4 mm^2 field of view. The mosaic pieces were acquired with 10%

overlap. Stitching[52] and reconstruction[51] operations were performed using Fiji[46] on the volumetric image segments. Fly-by videos were generated with the *Imaris* image analysis software (Bitplane, Belfast, United Kingdom).

Endothelial Functionality Assays: FITC labeled dextrans at two different molecular weights were introduced to microchannels with and without EC monolayer to quantify and visualize the endothelial barrier function. 20 kDa FITC–dextran (FD20, Sigma-Aldrich) and 200 kDa FITC–dextran (FD200, Sigma-Aldrich) solutions were prepared at 0.5 mg mL^{-1} end concentration in cell culture media. The solutions were added to the inlet reservoir of the respective microchannels individually. Fluorescence images were taken at 0 h (immediately after injection) and after 2 h using the 10× objective of Zeiss Axio Observer Z1 microscope (Zeiss). The permeability of microchannels was assessed by analyzing the diffusion of FITC probes into the hydrogel matrix. The average integrated density (*Av. IntDen*) of 20 different equal regions from each sample's microchannel and hydrogel matrix was measured using Fiji.[46] The following equation was used to calculate the diffusion percentage:

$$\text{Diffusion}(\%) = \frac{Av.\text{IntDen (Hydrogel Matrix)}}{Av.\text{IntDen (Hydrogel Matrix)} + Av.\text{IntDen (Microchannel)}} \times 100 \quad (3)$$

The effects of TNF-α stimulation on endothelial protein expression were analyzed immunocytochemically. Commercially available Ibidi y-shaped slides were used as experiment control (Ibidi, Munich, Germany). ECs at 7×10^5 mL^{-1} were seeded inside the bifurcating y-shaped slides and grown until confluence. In parallel, endothelialized microchannels were prepared as mentioned above. Static and perfusion controls (without TNF-α) were prepared for both conditions. ECs were stimulated with TNF-α (PELOBiotech, Planegg, Germany) at 2.5 ng mL^{-1} for 3 h.[53] Afterward, ECs were fixed with 4% paraformaldehyde, followed by permeabilization with 0.2% Triton X-100 in PBS blocked with 1% fetal calf serum for 1 h at room temperature. Monoclonal antibodies against vascular cell adhesion molecule-1 (VCAM-1, 1:100) and E-selectin (Clone BBIG-E4, 1:100) from R&D Systems (Wiesbaden, Germany) were applied overnight at 4 °C. Secondary antibody staining was performed with anti-mouse IgG coupled to Alexa Fluor 488 at 1:250 dilution (Molecular Probes, Karlsruhe, Germany) for 1 h and samples washed with PBS before microscopy to remove the leftover staining solution. Images of Ibidi slides were obtained using Zeiss Axio Observer Z1 microscope (Zeiss), and endothelialized microchannels were imaged using an upright SP5X laser scanning confocal microscope (Leica Microsystems GmbH, Wetzlar, Germany) with a 20×/1.0 NA water immersion objective. Images representing the same conditions were taken at the same exposure time or laser power to quantify protein expression differences properly. For quantification purposes, MetaVue software was used (Molecular Devices, Munich, Germany). Background signals were subtracted for every sample, and thresholded protein expression levels were expressed as arbitrary fluorescence units.

Statistical Analysis: All experiments were repeated independently two times and ran in triplicates. Unless stated otherwise, data obtained from different assays are presented as mean ± standard error of mean (SEM). The analysis of differences in dextran diffusion between the samples was performed using one-way ANOVA followed by all pairwise multiple comparisons. The differences in adhesion molecule expression between static and perfused samples were evaluated using Mann–Whitney U-test for samples with non-parametric distribution or by *t*-test for samples with normal distribution. $p < 0.05$ was considered statistically significant. SigmaPlot 12.3 Software was used for statistical analyses.

Supporting Information

Supporting Information is available from the Wiley Online Library or from the author.

Acknowledgements

M.R., H.G., and A.N. contributed equally. This study was funded by the Deutsche Forschungsgemeinschaft (DFG, German Research Foundation) – Project number 326998133 – TRR 225 (subprojects B02, B08, and A06) and supported by the ERC project Design2Flow (899609). The authors thank Beckmann (Dept. of Gynaecology, University Hospital Erlangen, Germany) for providing umbilical cords and the group of Barbara Dietel (Dept. of Cardiology, University Hospital Erlangen) for help with HUVEC isolation. The support of Ingo Thievessen (Biophysics Group, Faculty of Sciences, FAU) with confocal microscopy and of the Optical Imaging Centre Erlangen (OICE, FAU, Erlangen) with Thunder 3D imaging system is gratefully acknowledged. Leica Thunder Imager used for fluorescence microscopy was funded by Deutsche Forschungsgemeinschaft (DFG, German ResearchFoundation) — project 450993414.

Open access funding enabled and organized by Projekt DEAL.

Conflict of Interest

The authors declare no conflict of interest.

Data Availability Statement

The data that support the findings of this study are available from the corresponding author upon reasonable request.

Keywords

bifurcating microchannels, bioreactors, endothelial function, melt electrowriting, poly(2-oxazoline)

Received: January 20, 2022
Revised: April 29, 2022
Published online: June 7, 2022

[1] B. M. Baker, C. S. Chen, *J. Cell Sci.* **2012**, *125*, 3015.
[2] K. Duval, H. Grover, L. H. Han, Y. Mou, A. F. Pegoraro, J. Fredberg, Z. Chen, *Physiology* **2017**, *32*, 266.
[3] C. Mandrycky, K. Phong, Y. Zheng, *MRS Commun.* **2017**, *7*, 332.
[4] D. R. Grimes, C. Kelly, K. Bloch, M. Partridge, *J. R. Soc. Interface* **2014**, *11*, 20131124.
[5] W. G. Chang, L. E. Niklason, *npj Regener. Med.* **2017**, *2*, 7.
[6] G. Yang, B. Mahadik, J. Y. Choi, J. P. Fisher, *Prog. Biomed. Eng.* **2020**, *2*, 012002.
[7] Q. Wu, J. Liu, X. Wang, L. Feng, J. Wu, X. Zhu, W. Wen, X. Gong, *Biomed. Eng. Online* **2020**, *19*, 9.
[8] D. Therriault, S. R. White, J. A. Lewis, *Nat. Mater.* **2003**, *2*, 265.
[9] T. J. Hinton, Q. Jallerat, R. N. Palchesko, J. H. Park, M. S. Grodzicki, H. J. Shue, M. H. Ramadan, A. R. Hudson, A. W. Feinberg, *Sci. Adv.* **2015**, *1*, e1500758.
[10] C. Mota, D. Puppi, F. Chiellini, E. Chiellini, *J. Tissue Eng. Regener. Med.* **2015**, *9*, 174.
[11] L. Moroni, J. A. Burdick, C. Highley, S. J. Lee, Y. Morimoto, S. Takeuchi, J. J. Yoo, *Nat. Rev. Mater.* **2018**, *3*, 21.
[12] W. Wu, A. DeConinck, J. A. Lewis, *Adv. Mater.* **2011**, *23*, H178.
[13] D. B. Kolesky, K. A. Homan, M. A. Skylar-Scott, J. A. Lewis, *Proc. Natl. Acad. Sci. USA* **2016**, *113*, 3179.

[14] M. A. Skylar-Scott, S. G. Uzel, L. L. Nam, J. H. Ahrens, R. L. Truby, S. Damaraju, J. A. Lewis, *Sci. Adv.* **2019**, *5*, eaaw2459.
[15] J. Y. Ma, Y. C. Wang, J. Liu, *RSC Adv.* **2018**, *8*, 21712.
[16] M. K. Gelber, G. Hurst, T. J. Comi, R. Bhargava, *Addit. Manuf.* **2018**, *22*, 38.
[17] J. S. Miller, K. R. Stevens, M. T. Yang, B. M. Baker, D. H. Nguyen, D. M. Cohen, E. Toro, A. A. Chen, P. A. Galie, X. Yu, R. Chaturvedi, S. N. Bhatia, C. S. Chen, *Nat. Mater.* **2012**, *11*, 768.
[18] M. C. Gryka, T. J. Comi, R. A. Forsyth, P. M. Hadley, S. Deb, R. Bhargava, *Addit. Manuf.* **2019**, *26*, 193.
[19] G. Hochleitner, J. F. Hümmer, R. Luxenhofer, J. Groll, *Polymer* **2014**, *55*, 5017.
[20] C. B. Dayan, F. Afghah, B. S. Okan, M. Yıldız, Y. Menceloglu, M. Culha, B. Koc, *Mater. Des.* **2018**, *148*, 87.
[21] A. Hrynevich, B. Ş. Elçi, J. N. Haigh, R. McMaster, A. Youssef, C. Blum, T. Blunk, G. Hochleitner, J. Groll, P. D. Dalton, *Small* **2018**, *14*, 1800232.
[22] G. Hochleitner, T. Jüngst, T. D. Brown, K. Hahn, C. Moseke, F. Jakob, P. D. Dalton, J. Groll, *Biofabrication* **2015**, *7*, 035002.
[23] I. Cicha, K. Beronov, E. L. Ramirez, K. Osterode, M. Goppelt-Struebe, D. Raaz, A. Yilmaz, W. G. Daniel, C. D. Garlichs, *Atherosclerosis* **2009**, *207*, 93.
[24] J. Wild, O. Soehnlein, B. Dietel, K. Urschel, C. D. Garlichs, I. Cicha, *Thromb. Haemostasis* **2014**, *112*, 183.
[25] A. Nadernezhad, M. Ryma, H. Genç, I. Cicha, T. Jüngst, J. Groll, *Adv. Mater. Technol.* **2021**, *6*, 2100221.
[26] T. M. Robinson, D. W. Hutmacher, P. D. Dalton, *Adv. Funct. Mater.* **2019**, *29*, 1904664.
[27] D. B. Kolesky, R. L. Truby, A. S. Gladman, T. A. Busbee, K. A. Homan, J. A. Lewis, *Adv. Mater.* **2014**, *26*, 3124.
[28] R. W. Moreadith, T. X. Viegas, M. D. Bentley, J. M. Harris, Z. H. Fang, K. Yoon, B. Dizman, R. Weimer, B. P. Rae, X. L. Li, C. Rader, D. Standaert, W. Olanow, *Eur. Polym. J.* **2017**, *88*, 524.
[29] M. M. Bloksma, C. Weber, I. Y. Perevyazko, A. Kuse, A. Baumgärtel, A. Vollrath, R. Hoogenboom, U. S. Schubert, *Macromolecules* **2011**, *44*, 4057.
[30] C. D. Murray, *Proc. Natl. Acad. Sci. USA* **1926**, *12*, 207.
[31] B. Moreau, B. Mauroy, *J. Rheol.* **2015**, *59*, 1419.
[32] V. G. Djonov, H. Kurz, P. H. Burri, *Dev. Dyn.* **2002**, *224*, 391.
[33] H. Kurz, K. Sandau, *Comments Theor. Biol.* **1997**, *4*, 261.
[34] W. C. Aird, *Pharmacol. Rep.* **2008**, *60*, 139.
[35] A. R. Pries, T. W. Secomb, P. Gaehtgens, *Pfluegers Arch.* **2000**, *440*, 653.
[36] C. C. Michel, *Cardiovasc. Res.* **1996**, *32*, 644.
[37] G. Egawa, S. Nakamizo, Y. Natsuaki, H. Doi, Y. Miyachi, K. Kabashima, *Sci. Rep.* **2013**, *3*, 1932.
[38] M. Simionescu, A. Gafencu, F. Antohe, *Microsc. Res. Tech.* **2002**, *57*, 269.
[39] W. C. Aird, *Crit. Care Med.* **2004**, *32*, S271.
[40] K. Urschel, I. Cicha, *Int. J. Interferon, Cytokine Mediator Res.* **2015**, *7*, 9.
[41] U. M. Chandrasekharan, M. Siemionow, M. Unsal, L. Yang, E. Poptic, J. Bohn, K. Ozer, Z. Zhou, P. H. Howe, M. Penn, P. E. DiCorleto, *Blood* **2007**, *109*, 1938.
[42] K. Urschel, A. Worner, W. G. Daniel, C. D. Garlichs, I. Cicha, *Clin. Hemorheol. Microcirc.* **2010**, *46*, 203.
[43] M. Klarhofer, B. Csapo, C. Balassy, J. C. Szeles, E. Moser, *Magn. Reson. Med.* **2001**, *45*, 716.
[44] I. D. Driver, M. Traat, F. Fasano, R. G. Wise, *Front. Neurosci.* **2020**, *14*, 415.
[45] T. G. Papaioannou, C. Stefanadis, *Hell. J Cardiol.* **2005**, *46*, 9.
[46] J. Schindelin, I. Arganda-Carreras, E. Frise, V. Kaynig, M. Longair, T. Pietzsch, S. Preibisch, C. Rueden, S. Saalfeld, B. Schmid, J. Y. Tinevez, D. J. White, V. Hartenstein, K. Eliceiri, P. Tomancak, A. Cardona, *Nat. Methods* **2012**, *9*, 676.
[47] H. Zakaria, A. M. Robertson, C. W. Kerber, *Ann. Biomed. Eng.* **2008**, *36*, 1515.
[48] C. Poon, *J. Mech. Behav. Biomed. Mater.* **2022**, *126*, 105024.
[49] A. R. Pries, D. Neuhaus, P. Gaehtgens, *Am. J. Physiol.: Heart Circ. Physiol.* **1992**, *263*, H1770.
[50] I. Cicha, M. Goppelt-Struebe, S. Muehlich, A. Yilmaz, D. Raaz, W. G. Daniel, C. D. Garlichs, *Atherosclerosis* **2008**, *196*, 136.
[51] D. Schneidereit, S. Nübler, G. Prölss, B. Reischl, S. Schürmann, O. J. Müller, O. Friedrich, *Light: Sci. Appl.* **2018**, *7*, 79.
[52] S. Preibisch, S. Saalfeld, P. Tomancak, *Bioinformatics* **2009**, *25*, 1463.
[53] K. Urschel, A. Worner, W. G. Daniel, C. D. Garlichs, I. Cicha, *Clin. Hemorheol. Microcirc.* **2010**, *46*, 203.